PURPOSE-LED PUBLISHING™

PAPER • OPEN ACCESS

Radiative recombination model for BiSeI microcrystals: unveiling deep defects through photoluminescence

To cite this article: Marc Dolcet Sadurni *et al* 2024 *J. Phys. Energy* **6** 045004

View the article online for updates and enhancements.

You may also like

Journal of Physics: Energy

PAPER

OPEN ACCESS

CrossMark

Radiative recombination model for BiSeI microcrystals: unveiling deep defects through photoluminescence

Marc Dolcet Sadurni[1,*] , Jüri Krustok[1] , Kristi Timmo[1] , Valdek Mikli[1] , Rokas Kondrotas[2] ,
Maarja Grossberg-Kuusk[1] and Marit Kauk-Kuusik[1]

[1] Department of Materials and Environmental Technology, Tallinn University of Technology, Ehitajate tee 5, Tallinn 19086, Estonia
[2] Department of Characterisation of Materials Structure, Center for Physical Sciences and Technology, Saulėtekio av. 3, Vilnius 10257, Lithuania
* Author to whom any correspondence should be addressed.

E-mail: marc.dolcet@taltech.ee

Abstract

Pnictogen chalcohalides are semiconductors that have emerged as promising materials for energy conversion due to their exceptional optoelectronic properties. Their electronic configuration (ns^2), particularly for Bi- and Sb-based compounds, can be a key factor in efficient carrier transport and defect tolerance, similarly, to Pb-perovskites. In the present study, the Bi-containing chalcohalide, bismuth selenoiodide (BiSeI) was synthesized via isothermal heat treatment of binary precursors in evacuated quartz ampoules. The synthesized BiSeI microcrystals exhibited a characteristic needle-like morphology and a near-stoichiometric composition. Both indirect and direct band gap energies of BiSeI were determined by ultraviolet–visible–near-infrared diffuse reflectance spectroscopy, with room temperature values of 1.17 eV and 1.29 eV, respectively. This study presents the first experimental investigation of the photoluminescence properties of BiSeI microcrystals resulting in a recombination model involving multiple defect states. This work provides valuable insights into the defect structure and recombination mechanisms within BiSeI, paving the way for further exploration of its potential in optoelectronic devices.

1. Introduction

The escalating global energy demand and the detrimental effects of climate change have highlighted the necessity for sustainable energy solutions. Among these, photovoltaic (PV) energy stands out as a viable and promising alternative. The development of efficient and cost-effective solar cell materials is crucial in the growth of PV technologies [1, 2]. New solar absorbers must exhibit excellent optoelectronic properties, a tunable band gap ideally between 1.1–1.5 eV [3], a high absorption coefficient, high carrier mobility and defect tolerance. These materials should also demonstrate stability under ambient conditions (including temperature, humidity, and light exposure) and must be non-toxic.

Heavy pnictogen chalcohalides represent a class of inorganic ternary semiconductors characterized by the general formula $A^V B^{VI} C^{VII}$, where A = Bi, Sb; B = S, Se; C = Br, I. These materials are formed by the combination of a pnictogen cation (A) and two anions, a chalcogen (B) and a halogen (C). They share a similar ns^2 outer electronic configuration (Bi^{3+}, Sb^{3+}) with perovskites [4, 5]. This electronic structure is believed to be closely linked to efficient carrier transport and good defect tolerance, which are key factors contributing to the high performance of perovskite solar cells [6]. Consequently, Bi and Sb-based chalcohalides are expected to exhibit similar optoelectronic properties, making them promising absorbers. They have been recently investigated and applied not only in PV applications [7–11] but also in photocatalysis, photodetectors [12], thermoelectric devices [13], and piezoelectric nanogenerators [11, 12, 14, 15] among other potential applications.

Among heavy pnictogen chalcohalides, bismuth selenoiodide (BiSeI) possess a high absorption coefficient ($\sim 10^{-5}$ cm^{-1}) [16] and a narrow band gap of 1.29 eV [17]. Density functional theory

calculations indicate a small difference between the direct and indirect band gap energies of BiSeI, reported as 0.02 eV in [18] and 0.1 eV in [19]. This material crystallizes in the orthorhombic crystal structure [20] with *Pnma* (62) space group [4]. Similarly to other pnictogen chalcohalides, the structure of BiSeI consists of double chains of $(Bi_2Se_2I_2)_n$. Within these ribbons, Bi and Se atoms exhibit strong covalent bonding, while iodine ions are bonded ionically with a covalently bound bridge [21]. Neighboring ribbons are linked by weak van der Waals forces [17], resulting in a layered structure.

Several synthesis methods have been explored for BiSeI materials, including physical vapor transport [17, 21–23], solution-based growth [24], ball milling [25] etc. The used synthesis method significantly influences the electrical conductivity type and defect structure of BiSeI crystals. The stoichiometry during growth plays a crucial role in determining the nature and concentration of defects within the crystal lattice of BiSeI. Anion-rich conditions (excess of Se and I) are likely to promote the formation of acceptor-like defects, such as Se_{Bi}, V_{Bi}, while Bi-rich environments favor the creation of donor-like defects, such as Bi_{Se}, V_I, V_{Se} and Bi_i [18].

Despite the promising optoelectronic properties of BiSeI, no experimental data is currently available regarding its defect structure. In this study, the optical properties of BiSeI, particularly the band gap energies, were determined. Due to the limited understanding of BiSeI's defect structure and recombination mechanisms, a photoluminescence (PL) study was conducted at different temperatures and laser excitation powers to experimentally investigate these aspects.

2. Experimental details

BiSeI microcrystals used in this study were synthesized via a solid-state method, using self-prepared Bi_2Se_3 and commercially available BiI_3 (Aldrich, 99%). The precursors were used in a molar ratio of Bi : Se : I = 1 : 1 : 1, calculated based on the masses of the binary precursors and weighed to achieve a total mass of 1 g according to the reaction formula: $Bi_2Se_3 + BiI_3 \rightarrow 3BiSeI$.

The mixture of precursors was finely ground in an agate mortar to achieve uniformity and facilitate the reaction. The homogeneous mixture was transferred into a quartz ampoule with dimensions of 6.5 cm in length and 1.2 cm in diameter. The ampoule was then subjected to dynamic vacuum degassing and sealed. It was gradually heated from room temperature (RT) to 225 °C within 3 h. After maintaining this temperature for 24 h, the temperature was further increased from 225 °C to 440 °C within 5 h. The material was held at 440 °C for 256 h before being cooled down to RT by removing the ampoule from the furnace to ambient conditions.

The morphology of BiSeI microcrystals was investigated using a high-resolution scanning electron microscope (HR-SEM Zeiss Merlin). For detailed surface imaging, a high-efficiency In-lens secondary electron detector was used. To achieve compositional contrast, an energy-selective backscattered electron detector was utilized. The chemical composition of individual crystals was analyzed using x-ray dispersive spectroscopy (EDX) with a Bruker Esprit 1.82 system with an EDX-XFlash 3001 detector. Polished samples revealing the bulk of the crystals was examined using an accelerating voltage of 20 kV. X-ray diffraction (XRD) was the technique selected to characterize the crystal structure of BiSeI microcrystals. A Rigaku Ultima IV diffractometer utilizing monochromatic Cu Kα radiation ($\lambda = 1.5406$ Å, 40 kV, 40 mA and a silicon strip detector (D/teX Ultra) was used. Phase identification and calculation of lattice parameters were performed using PDXL2 Rigaku software. The phase composition of BiSeI microcrystals was further investigated by RT micro-Raman spectroscopy. A Horiba`s LabRam HR 800 spectrometer equipped with a cooled multichannel CCD detector in a backscattering configuration was utilized to carry out the measurements. The YAG: Nd 532 nm laser with a power density of 13 kW cm^{-2} was focused on the individual crystals. The same equipment was used to perform RT-PL measurements. ultraviolet–visible–near-infrared (UV–Vis–NIR) diffuse reflectance was measured using Shimadzu UV-3600 two-beam spectrometer equipped with a multi-purpose compartment MPC-3100. Samples were placed in a 60 mm integrating sphere and a barium sulphate target was used for calibration. Measurements were recorded between 260 and 2600 nm. For temperature-dependent PL measurements, BiSeI single crystals were placed on the cold finger of the closed-cycle helium cryostat (Janis CCS-150). Then its temperature was decreased to 8 K. The temperature was adjusted up to 200 K via a temperature controller (LakeShore Model 335). PL excitation was achieved using a 532 nm Cobolt 08-DPL laser. The power density of the incident laser beam was altered via neutral density filters between 0.04 and 0.3 W cm^{-2}. An optical chopper was used for modulating the laser light. The resulting luminescence was filtered through a cut-off low-pass filter and then directed towards a computer-controlled single grating (600 lines mm^{-1}) monochromator ($f = 0.64$ m) (Horiba Jobin Yvon FHR640). Two different detectors were used, R632 and InGaAs photomultiplier tubes (PMT). A Stanford SR810 DSP lock-in amplifier was employed to amplify the PL signal.
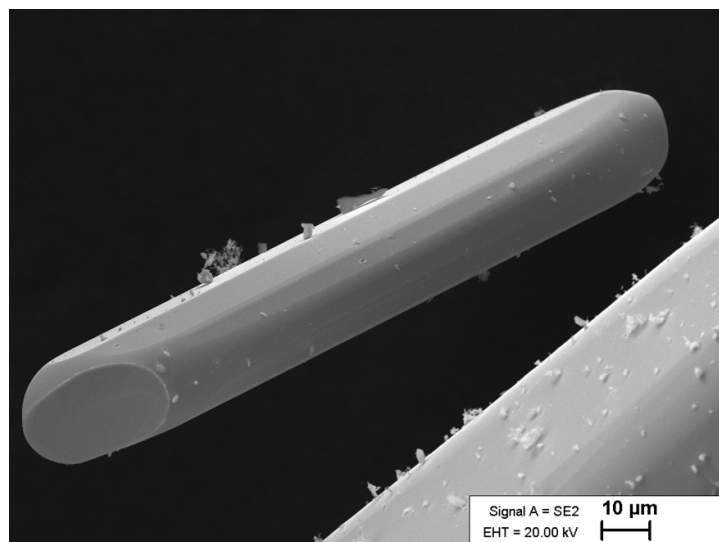
Figure 1. SEM image of a single needle-like BiSeI microcrystal.

3. Results and discussion

3.1. Elemental and phase composition of BiSeI microcrystals

SEM studies of the synthesized microcrystals (figure 1) showed the formation of needle-like crystals, consistent with previous reports on BiSeI [17] and similar to other pnictogen chalcohalides [26, 27]. These crystals exhibit variations in both thickness and length, reflecting the anisotropic growth behaviour of BiSeI. Crystal lengths range from tens of micrometers to several centimeters, while their thickness typically remains below 500 μm. EDX analysis of the bulk of the microcrystals revealed an average composition of 34.1 at% of Bi, 32.7 at% of Se, and 33.2 at% of I. This composition closely corresponds to the expected stoichiometric ratio of 1:1:1 (33.3 at% for each element), confirming the successful synthesis of BiSeI.

In figure 2(a), the XRD pattern of the synthesized BiSeI microcrystals is shown. The diffraction peaks were compared to the reference pattern of BiSeI (ICDD 01-070-4693). The analysis indicated that the majority of the observed diffraction peaks align with the orthorhombic crystal structure with the space group *Pnma* (62). This excellent agreement with the reference pattern confirms that BiSeI is the predominant phase present in the synthesized microcrystals. However, to some extent, the presence of Bi_2Se_3 (ICDD 01-077-7147) as a secondary phase was identified. These secondary phase peaks were located at 2θ values of 18.6°, 28.1° and 37.7°. Calculated lattice parameters of BiSeI were following: $a = 8.6956(5)$ Å, $b = 4.2155(9)$ Å, $c = 10.5715(5)$ Å, which are in agreement with previous reports [25, 28]. The phase composition of individual BiSeI microcrystals was also investigated using Raman spectroscopy. The Raman spectrum, shown in figure 2(b), was fitted using Lorentzian functions to resolve the peaks. The analysis revealed Raman peaks at 75, 96, 105, 115, 137, 153, 159, 182 and 186 cm^{-1}, which are in a good agreement with previously reported Raman data of BiSeI [29]. Raman peaks at 153, 159, 182 and 186 cm^{-1} are associated with Bi-Se, while peaks at 75 and 96 cm^{-1} with Bi-I vibration modes [30–32]. Raman measurements were done from different grains and different spots. No secondary phase peaks corresponding to Bi_2Se_3 [33, 34] could be detected in the Raman spectrum. Although minor residual amounts of Bi_2Se_3 were detected in the final product by XRD, the overall composition of the synthesized BiSeI microcrystals remains predominantly pure, as confirmed by EDX and Raman analyses. This discrepancy may be attributed to the use of a polycrystalline form of BiSeI powder material for the XRD analysis, while single, carefully selected crystals were used for the Raman and PL measurements. Consequently, the presence of traces of Bi_2Se_3 is unlikely to significantly impact the bulk PL response. Furthermore, the band gap energy of Bi_2Se_3 single crystals has been reported to be between 0.22 eV [35] and 0.33 eV [36]. This significant difference in band gap makes it highly unlikely that any PL band observed in the PL spectra of BiSeI can be attributed to Bi_2Se_3.

3.2. Optical properties of BiSeI microcrystals

UV–Vis–NIR diffuse reflectance measurements were performed on BiSeI microcrystals to determine the optical band gap. The band gap energy of BiSeI microcrystals was determined using the Kubelka–Munk
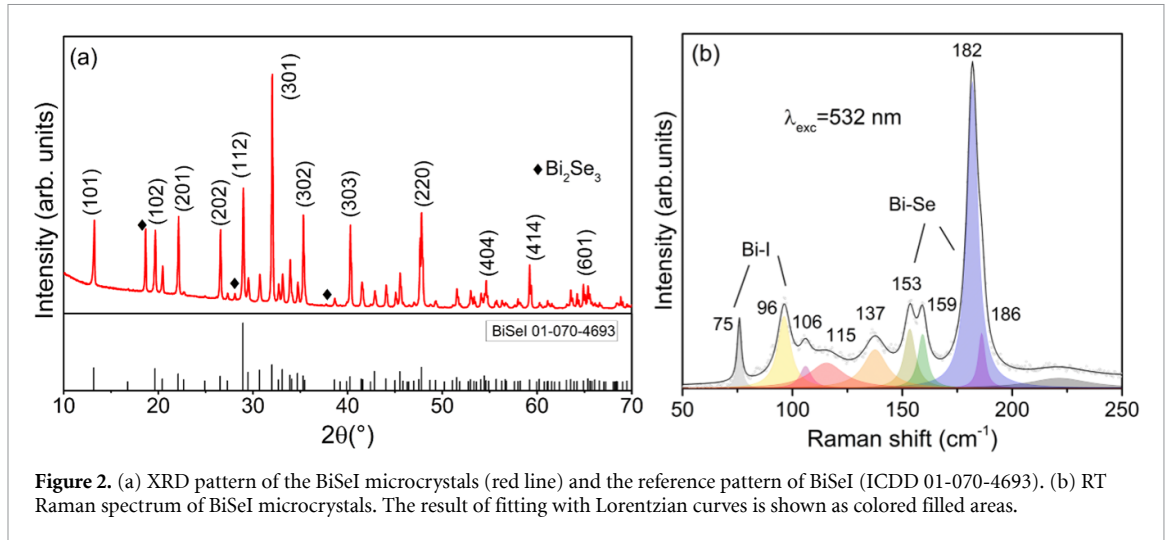
Figure 2. (a) XRD pattern of the BiSeI microcrystals (red line) and the reference pattern of BiSeI (ICDD 01-070-4693). (b) RT Raman spectrum of BiSeI microcrystals. The result of fitting with Lorentzian curves is shown as colored filled areas.

theory [37]. The band gap energy was estimated by fitting the data according to the Tauc equation:

$$(\alpha h\nu)^{1/n} = A\left(h\nu - E_g\right) \tag{1}$$

where α is the absorption coefficient, h is the Planck constant, ν is the photon's frequency of vibration, A is a proportional constant, E_g is the band gap energy and the value of the n exponent indicates the nature of the optical transition, $1/2$ for direct and 2 for indirect transition. The diffuse reflectance spectrum can be converted to Kubelka–Munk function by quantifying $F(R_\infty)$, in the limiting case of an infinitely thick sample, which is proportional to α [37],

$$F(R_\infty) = \frac{(1 - R_\infty)^2}{2R_\infty} \sim \alpha \tag{2}$$

where R_∞ is the absolute diffuse reflectance. Then,

$$(F(R_\infty)h\nu)^{1/n} = A\left(h\nu - E_g\right). \tag{3}$$

A tangent line can be drawn from the linear part of the function to zero to determine the band gap energy of BiSeI, as shown in figure 3. Direct band gap value of $E_g = 1.29$ eV and indirect band gap value of $E_g = 1.17$ eV were obtained. The determined indirect band gap aligns well with previous report [30]. However, it should be noted that $[F(R_\infty)h\nu]^{1/2}$ does not converge to 0 when $h\nu$ decreases. This limitation suggests that it is not possible to be completely certain about the precise value of the indirect band gap energy. Nevertheless, the observed difference of 0.12 eV between the direct and indirect band gaps is consistent with prior theoretical calculations for BiSeI [19].
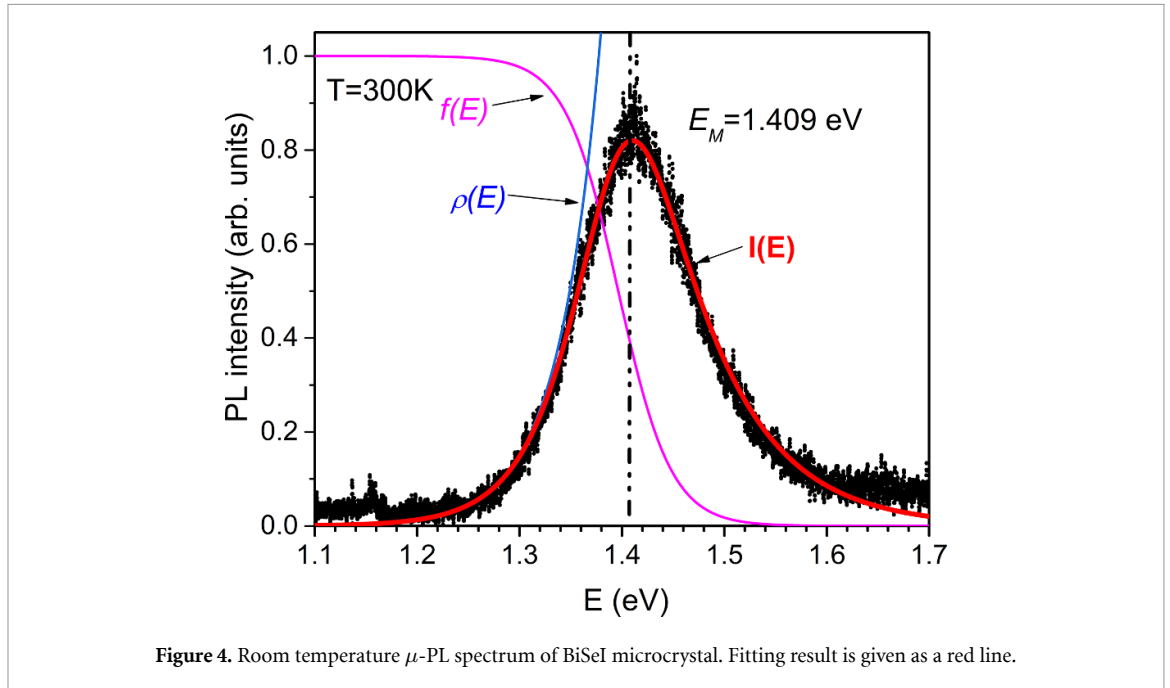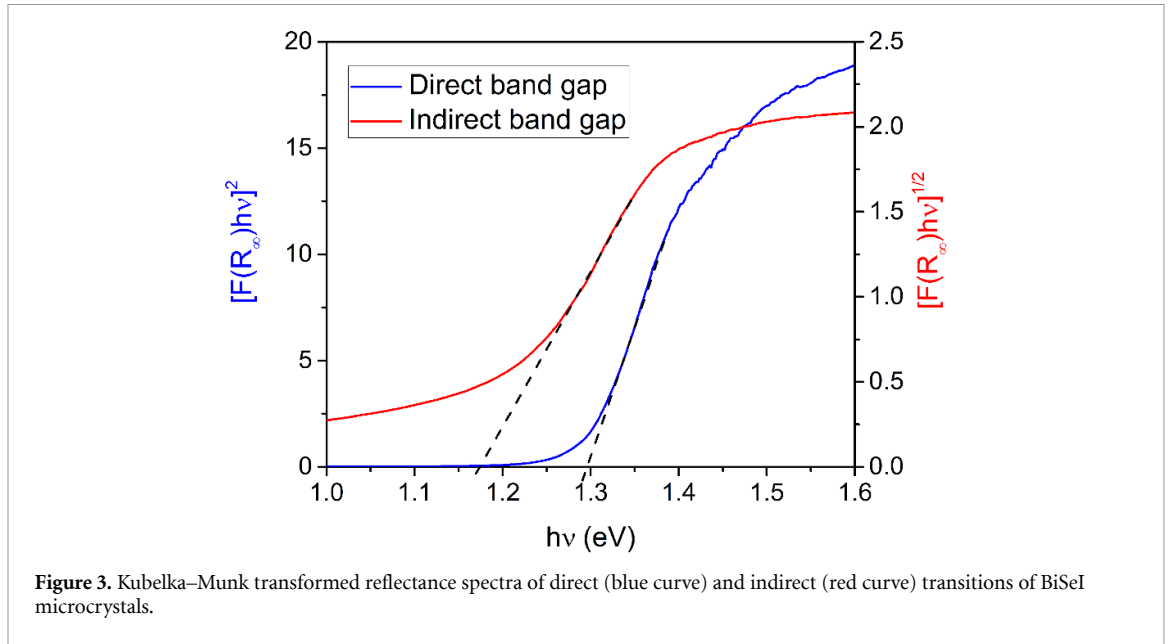
The room-temperature μ-PL spectrum of the BiSeI microcrystal showed only one slightly asymmetric band (see figure 4). The PL intensity of this band was quite low even at very high laser power density ($\sim$13 kW cm^{-2}). This maximum laser power density was selected to ensure that the Raman or PL spectra of the sample remained unchanged. The rise in intensity from the high energy side of the band is rather gentle compared to the more abrupt fall from the low energy side. This type of PL band shape is typical for band-to-band (BB) recombination, where the shape of the high energy side is determined by the Fermi distribution function

$$f(E) = \left[1 + \exp\left((E - E_F)/kT\right)\right]^{-1} \tag{4}$$

and the shape of the low energy side is related to the density of states function $\rho(E)$ [38–40]. The nearly exponential low energy side of the BB-band of studied crystal suggests that the defect density is quite large, resulting in the creation of exponential Urbach-like tail states. Therefore, the $\rho(E)$ function has a form
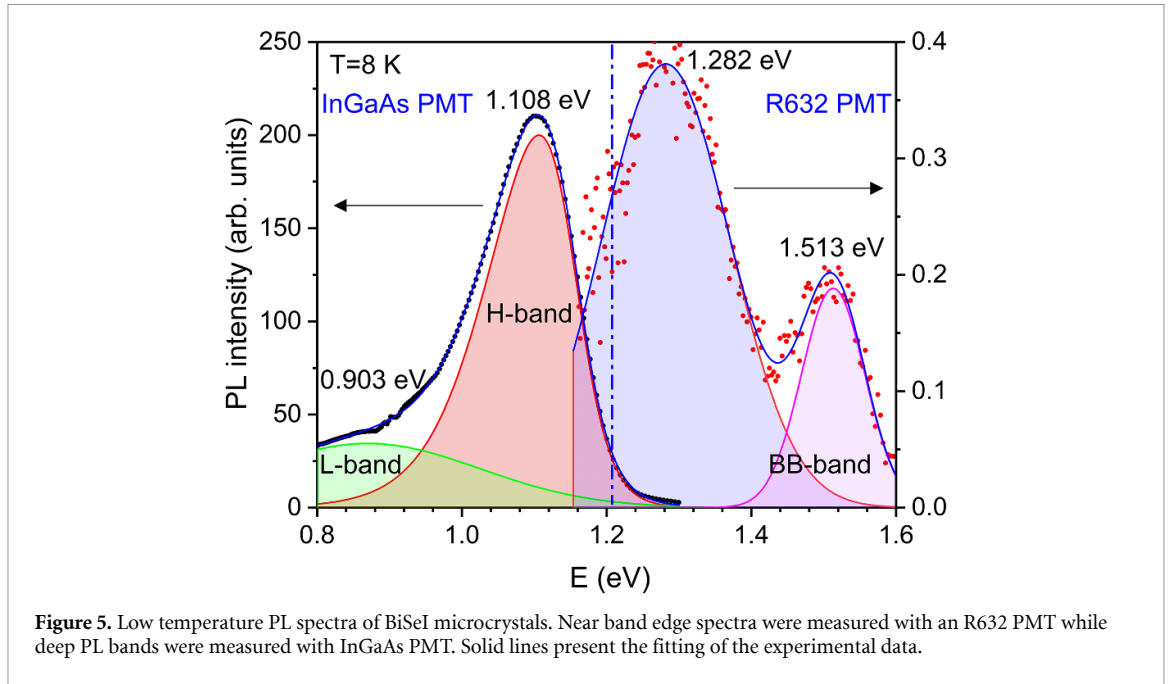
$$\rho(E) = \rho_0 \exp\left[(E - E_g)/E_u\right], \tag{5}$$

where E_g is the band gap energy, and E_U is the characteristic Urbach energy that scales the extent of the Urbach tail density of localized defect states in the gap; ρ_0 is an amplitude factor [40]. Consequently,

Figure 3. Kubelka–Munk transformed reflectance spectra of direct (blue curve) and indirect (red curve) transitions of BiSeI microcrystals.

Figure 4. Room temperature μ-PL spectrum of BiSeI microcrystal. Fitting result is given as a red line.

$I(E) = f(E) * \rho(E)$ function was used to fit RT BB-band shape. The result of this fitting is given in figure 4 as a continuous line. The best fit was obtained using the following values: $E_F = 1.396$ eV, $E_g = 1.336$ eV, $E_U = 41$ meV, and $T = 300$ K. The peak position of the BB-band is measured at $E_M = 1.409$ eV. Even though the peak position of the BB-band varies with temperature and excitation intensity, it is frequently used to calculate the band gap energy E_g. In this case, due to the quite high excitation intensity, it is expected that the real band gap energy is lower than the peak position E_M. Although there is a 73 meV difference between these values, it must be considered that the density of states function could have a more complex structure. As a result, the shape of BB-band can only provide a rough estimation of the value of E_g. Moreover, the intensity of this BB-band was very weak, which can be attributed to the presence of both indirect and direct band gaps. In that case, the low energy side of the BB-band may have an even more intricate shape. Nevertheless, the RT band gap value obtained from the fitting is very close to the theoretically calculated value $E_g = 1.31$ eV [18].

However, the band gap energy obtained from the RT-PL measurements is higher (about 46 meV) than the same energy obtained from reflectance measurements. In this case, state-filling of band edge states occurs due to very high excitation power. A similar effect was observed by Fang *et al* where the BB-band exhibited a blueshift with increasing laser power [41].

Figure 5. Low temperature PL spectra of BiSeI microcrystals. Near band edge spectra were measured with an R632 PMT while deep PL bands were measured with InGaAs PMT. Solid lines present the fitting of the experimental data.

As shown in figure 5, low temperature ($T = 8$ K) PL measurements identified four distinct PL bands. BB emission was measured using an R632 PMT and two very weak PL bands were detected. Both bands were fitted using Gaussian function. The PL band at 1.513 eV is nearly identical to the 0 K direct band gap value of $E_g = 1.52$ eV calculated in [18], indicating that BB recombination is associated with this band. Anticipating that the BB peak position will now be closer to the band gap value due to the relatively low laser power density ($\sim$0.3 W cm^2). Using the RT value of $E_g = 1.336$ eV and the experimentally determined rate of temperature dependence of E_g ($\mathrm{d}E_g/\mathrm{d}T = -6.5 * 10^{-4}$eVK^{-1}) [42], it is also possible to derive the low temperature E_g value of 1.52 eV.
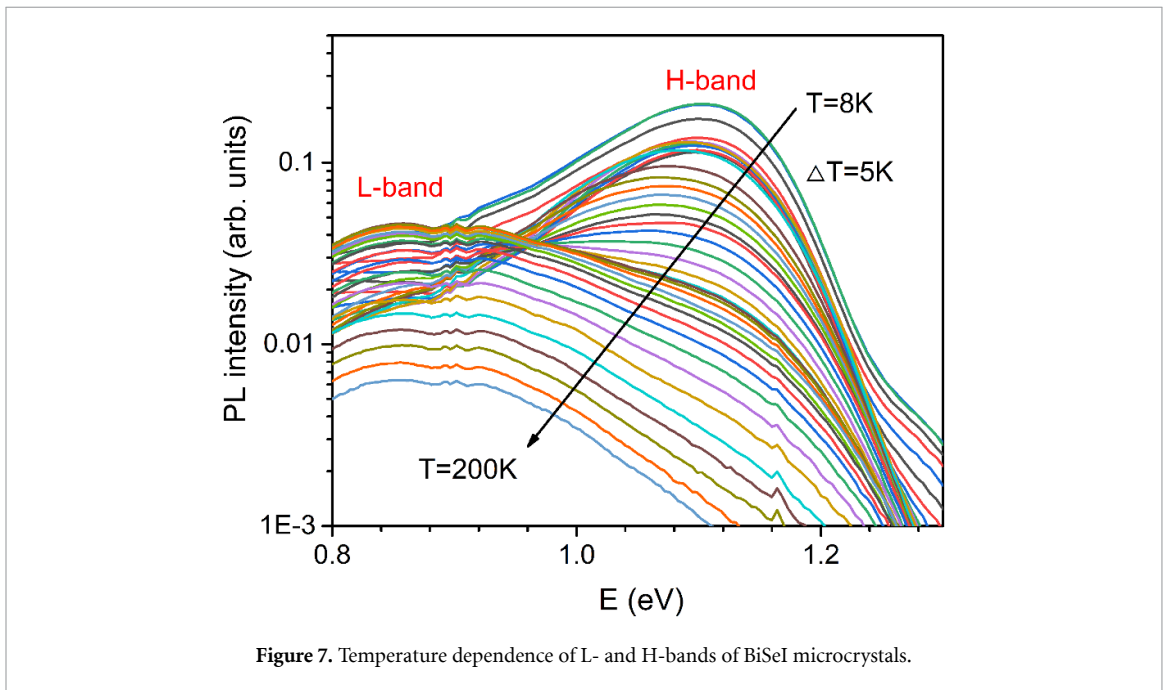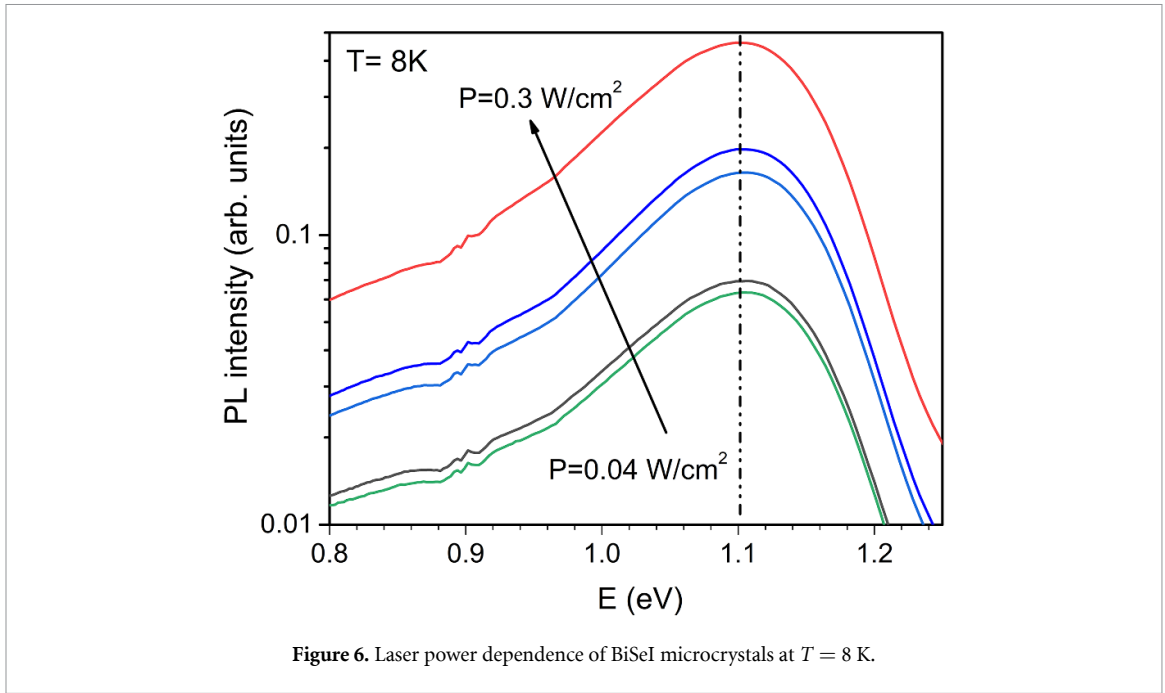
Unfortunately, a thorough examination of this BB-band was hindered by its extremely low intensity. The deeper PL band at 1.282 eV also exhibited the same issue. Unfortunately, the origin of this band cannot be determined.

Two deeper bands with relatively high intensity were observed by using the InGaAs PMT. They are referred to as the H-band ($E_M = 1.108$ eV) and L-band ($E_M = 0.903$ eV). It is evident that these bands are associated with different types of recombination. Due to the asymmetric shape of the H-band, the data was fitted using the asymmetric double sigmoidal function. Since the L-band was less pronounced, it was fitted with a Gaussian function. All the fitting results are shown in figure 5.

The laser power and temperature dependence of synthesized BiSeI microcrystals could be measured due to the high PL starting intensity. Figure 6 shows the laser power dependence. It is evident that both the general shape of the L- and H-bands and the peak position of the H-band remain unchanged with increasing laser power. This suggests that both bands have similar origins.

The H- and L-band temperature dependence is displayed in figure 7. At lower temperatures, the H-band predominates, whereas at higher temperatures, the L-band begins to dominate. It indicates that the thermal activation energies of the two PL bands are not the same. Indeed, figure 8 shows the Arrhenius plot for both PL bands. The higher temperature part was fitted using a simple function $\Phi = \Phi_0 / [1 + \alpha \exp(E_a/kT)]$, where E_a is a thermal activation energy, ϕ is the integral intensity of PL band, and α is a fitting constant. The activation energies that were obtained are relatively close to each other, see figure 8. At the same time, there is more rapid quenching of the H-band, as shown in figure 7. This is possible if the values of parameter α are different for both PL bands. The parameter α is proportional to the probability of electronic transition from a localized donor level to a delocalized band, and a higher value of α leads to more rapid quenching of the PL band [43]. Indeed, the α values are $7.8*10^6$ and $2.2*10^5$ for the H- and L-band, respectively. Different values of α are probably related to different donor defects of DD-DA pairs.
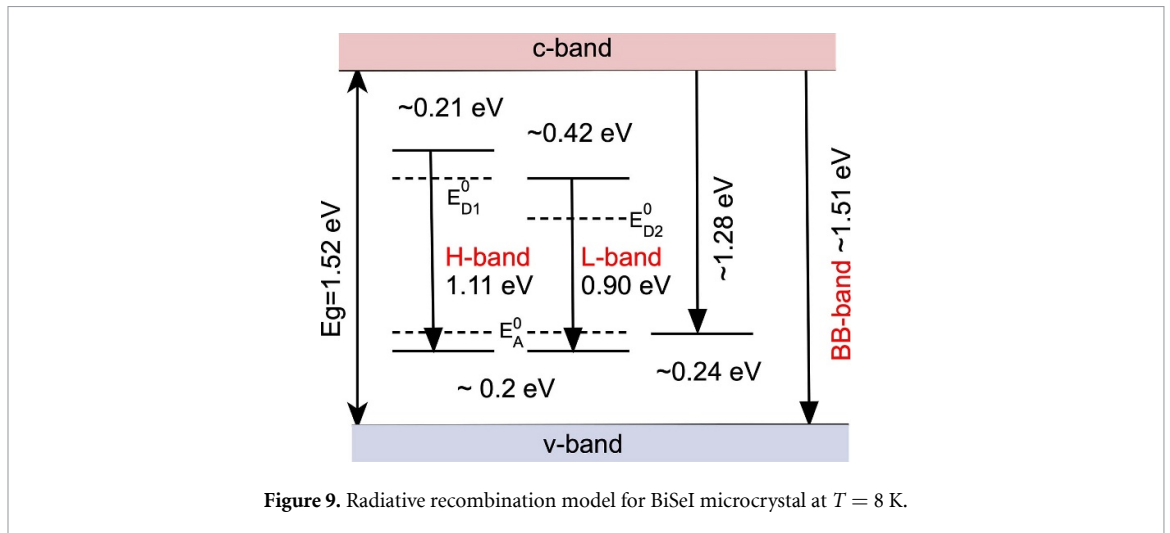
The peak positions of both deep PL bands are distant from the band gap energy. General distant donor-acceptor pair recombination model and recombination involving Urbach tail states can be ruled out due to the relatively low E_a values and the absence of peak position shift with increasing laser intensity. Similar conditions have been found in many other semiconductor compounds, and recombination between discrete levels that are far from band edges is frequently cited as the cause. The temperature and laser power

Figure 6. Laser power dependence of BiSeI microcrystals at $T = 8$ K.

Figure 7. Temperature dependence of L- and H-bands of BiSeI microcrystals.

dependencies of both bands suggest that these bands may be related to deep donor-deep acceptor (DD-DA) complexes. The DD-DA pair model was initially proposed to explain similar behavior of deep PL bands in CdTe [44] and in various chalcopyrites [45–47]. Because the electron and hole wave functions are localized in these deep levels, PL emissions from these DA pairs can only be seen at smallest separation between donor and acceptor defects. In this model the emission energy from a DA pair separated by a distance *r* is obtained from [47]

$$E(r) = E_g - \left(E_A^0 + E_D^0\right) + \frac{e^2}{\varepsilon r} - \Gamma(r), \tag{6}$$

where E_g is the band gap energy, E_A^0 and E_D^0 are the acceptor and donor ionization energies, ε is the dielectric constant, and $\Gamma(r)$ refers to interactions that are only important at extremely short distances. However, as Williams [48] demonstrated, in the case of extremely short donor-acceptor distances, the magnitude of $\Gamma(r)$ may be greater than or equal to 25 meV.

Figure 8. Arrhenius plots derived from the temperature dependence of PL spectra together with the obtained thermal activation energy values, E_a.

Figure 9. Radiative recombination model for BiSeI microcrystal at $T = 8$ K.
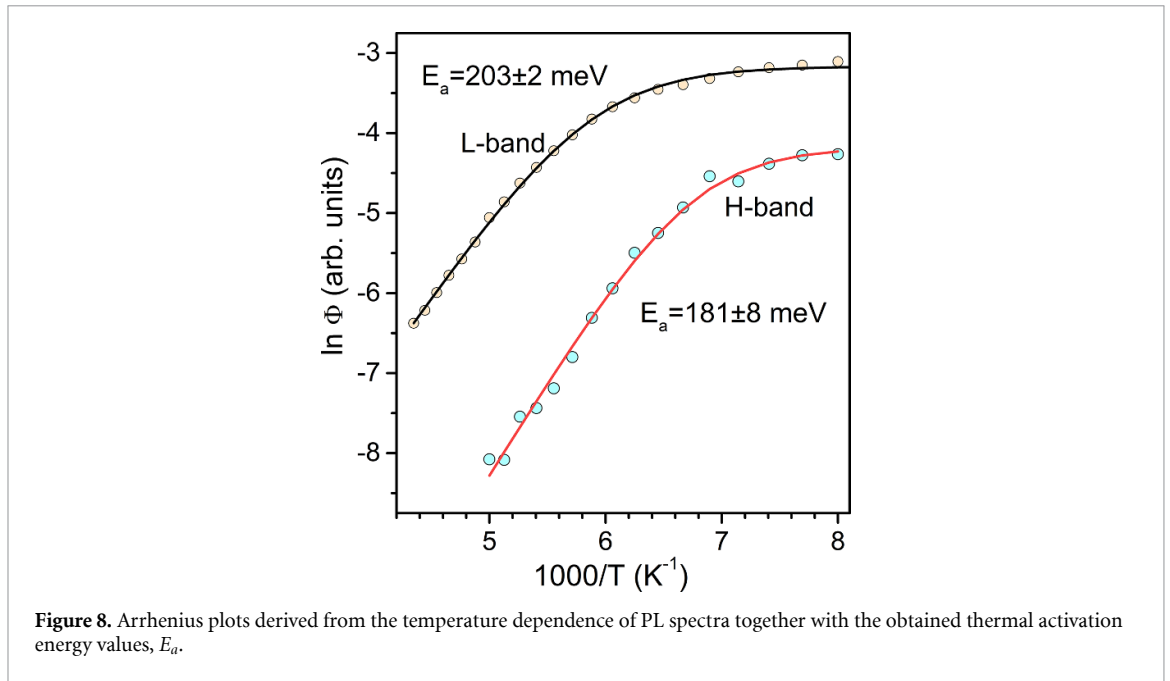
As a result, the Coulombic energy determined theoretically typically tends to be slightly higher than the energy observed experimentally. Although the precise value of the dielectric constant in BiSeI is unknown, estimates place it at approximately 35 [6]. The shortest distance between different lattice sites in BiSeI is between Bi and Se sites, where $r = 2.74$ Å [19]. So, the highest value of the Coulomb term in BiSeI is about 150 meV. Moreover, in the spaces between the one-dimensional ribbons, two interstitial defect sites are present: one penta-coordinated site and one octa-coordinated site. So, iodine on chalcogen antisite (I_{Se}), anion on bismuth antisites (Se_{Bi} and I_{Bi}), anion vacancies (V_I and V_{Se}), bismuth interstitial (Bi_i), a bismuth vacancy (V_{Bi}), Se on iodine antisite (Se_I), bismuth on Se and I antisites (Bi_{Se} and Bi_I), and anion interstitials (Se_i and I_i) can be found in BiSeI crystals [18]. Unfortunately, there is a lack of experimental information on potential defects in BiSeI; however, theoretical defect energy calculations were carried out by Ganose *et al* [18] The PL data from this study indicates that the H-band and L-band may be associated with the same DA defect, which has an activation energy of approximately 0.2 eV. A weak edge emission band at 1.282 eV, is also most likely associated with the same acceptor defect. According to the computation results provided by Ganose *et al*, the most suitable acceptor defect is V_{Bi}. At the same time, DD defects for the H- and L-bands are different. There are several DD defects present in BiSeI crystals. The most appropriate defects are Se_{Bi} and interstitial I_i with both coordination symmetry [18]. Further research will be necessary to determine the exact origin of the DD defects in the H- and L-bands, as there is currently significant uncertainty in this area. As a result of this study, the radiative recombination model for BiSeI crystals is presented in figure 9.

4. Conclusion

BiSeI microcrystals with a needle-like morphology were successfully synthesized via a solid-state method using Bi_2Se_3 and BiI_3 precursors. The formation of BiSeI predominantly as a single phase was confirmed by Raman spectroscopy and XRD. The synthesized material exhibited a composition close to stoichiometric (Bi : Se : I = 1 : 0.96 : 0.97) and crystallized in an orthorhombic structure with the *Pnma* (62) space group. RT indirect band gap of 1.17 and direct band gap of 1.29 eV were determined from the UV–Vis–NIR reflectance spectra of BiSeI microcrystals. The comprehensive PL study revealed a complex defect structure in BiSeI microcrystals. At 8 K, four distinct PL bands have been observed. The H- and L-bands are attributed to DD-DA pairs, while the band at 1.282 eV is likely related to a deep defect with an ionization energy of 240 meV. These three bands may be associated with a bismuth vacancy defect. Additionally, DD defects contributing to the H- and L-bands could be identified as Se_{Bi} and interstitial I_i. Finally, BB-band is attributed to a BB recombination. The identification of these defect states provides crucial insights into the radiative recombination pathways, which is essential for optimizing material performance. However, further research is needed to accurately identify the origin of DD defects in the H- and L-bands.

Data availability statement

All data that support the findings of this study are included within the article (and any supplementary files).

Conflict of interest

The authors declare that they have no known competing financial interests or personal relationships that could have appeared to influence the work reported in this paper.

ORCID iDs

Marc Dolcet Sadurni ● https://orcid.org/0000-0003-0821-1550
Jüri Krustok ● https://orcid.org/0000-0002-4671-2332
Kristi Timmo ● https://orcid.org/0000-0001-6054-6783
Valdek Mikli ● https://orcid.org/0000-0002-2406-3562
Rokas Kondrotas ● https://orcid.org/0000-0002-1751-7909
Maarja Grossberg-Kuusk ● https://orcid.org/0000-0003-3357-189X
Marit Kauk-Kuusik ● https://orcid.org/0000-0003-0071-8568

References

[1] Wang K, Xu Z, Guo Z, Wang H, Qaid S M H, Yang K and Zang Z 2024 Phosphonate diacid molecule induced crystallization manipulation and defect passivation for high-performance inverted MA-free perovskite solar cells *Adv. Energy Mater.* **14** 2402249
[2] He T, Jiang Y, Xing X and Yuan M 2020 Structured perovskite light absorbers for efficient and stable photovoltaics *Adv. Mater.* **32** 1–17
[3] Bremner S P, Yi C, Almansouri I, Ho-Baillie A and Green M A 2016 Optimum band gap combinations to make best use of new photovoltaic materials *Sol. Energy* **135** 750–7
[4] Brandt R E, Stevanović V, Ginley D S and Buonassisi T 2015 Identifying defect-tolerant semiconductors with high minority-carrier lifetimes: beyond hybrid lead halide perovskites *MRS Commun.* **5** 265–75
[5] Grandhi G K, Hardy D, Krishnaiah M, Vargas B, Al-Anesi B, Suryawanshi M P, Solis-Ibarra D, Gao F, Hoye R L Z and Vivo P 2023 Wide-bandgap perovskite-inspired materials: defect-driven challenges for high-performance optoelectronics *Adv. Funct. Mater.* 2307441
[6] Shi H, Ming W and Du M H 2016 Bismuth chalcohalides and oxyhalides as optoelectronic materials *Phys. Rev.* B **93** 1–7
[7] Hahn N T, Self J L and Mullins C B 2012 BiSI micro-rod thin films: efficient solar absorber electrodes? *J. Phys. Chem. Lett.* **3** 1571–6
[8] Choi Y C and Jung K W 2020 Recent progress in fabrication of antimony/bismuth chalcohalides for lead-free solar cell applications *Nanomaterials* **10** 1–15
[9] Nie R, Hu M, Risqi A M, Li Z and Seok S I 2021 Efficient and stable antimony selenoiodide solar cells *Adv. Sci.* **8** 1–8
[10] Nie R, Im J and Seok S I 2019 Efficient solar cells employing light-harvesting Sb 0.67 Bi 0.33 SI *Adv. Mater.* **31** 1–8
[11] Nie R and Seok S I 2020 Efficient antimony-based solar cells by enhanced charge transfer *Small Methods* **4** 1–10
[12] Farooq S, Feeney T, Mendes J O, Krishnamurthi V, Walia S, Della Gaspera E and van Embden J 2021 High gain solution-processed carbon-free BiSI chalcohalide thin film photodetectors *Adv. Funct. Mater.* **31** 1–13

[13] Peng B, Xu K, Zhang H, Ning Z, Shao H, Ni G, Li J, Zhu Y, Zhu H and Soukoulis C M 2018 1D SbSeI, SbSI, and SbSBr with high stability and novel properties for microelectronic, optoelectronic, and thermoelectric applications *Adv. Theory Simul.* **1** 1–7

[14] Purusothaman Y, Alluri N R, Chandrasekhar A and Kim S J 2018 Photoactive piezoelectric energy harvester driven by antimony sulfoiodide (SbSI): a AVBVICVII class ferroelectric-semiconductor compound *Nano Energy* **50** 256–65

[15] Toroń B, Mistewicz K, Jesionek M, Kozioł M, Zubko M and Stróż D 2022 A new hybrid piezo/triboelectric SbSeI nanogenerator *Energy* **238** 122048

[16] Shin D-W, Hyun S-C, Park S-A, Kim Y-G, Chang-dae K and Kim W-T 1994 Optical properties of undoped and Ni-doped VA-VIA-VIIA single crystals *J. Phys. Chem. Solids* **55** 825–30

[17] Xiao B, Zhu M, Ji L, Zhang B B, Dong J, Yu J, Sun Q, Jie W and Xu Y 2019 Centimeter size BiSeI crystal grown by physical vapor transport method *J. Cryst. Growth* **517** 7–11

[18] Ganose A M, Matsumoto S, Buckeridge J and Scanlon D O 2018 Defect engineering of earth-abundant solar absorbers BiSI and BiSeI *Chem. Mater.* **30** 3827–35

[19] Ganose A M, Butler K T, Walsh A and Scanlon D O 2016 Relativistic electronic structure and band alignment of BiSI and BiSeI: candidate photovoltaic materials *J. Mater. Chem.* A **4** 2060–8

[20] Wlaźlak E *et al* 2018 Heavy pnictogen chalcohalides: the synthesis, structure and properties of these rediscovered semiconductors *Chem. Commun.* **54** 12133–62

[21] Audzijonis A, Gaigalas G, Žigas L, Sereika R, Žaltauskas R, Balnionis D and Reza A 2009 Electronic structure and optical properties of BiSeI crystal *Phys. Status Solidi b* **246** 1702–8

[22] Arivuoli D, Gnanam F D and Ramasamy P 1987 Growth of bismuth seleno iodide single crystals from the vapour *J. Mater. Sci.* **22** 981–4

[23] An C, Du X, Chen X, Zhou Y, Zhang M, Zhou Y, Zhou J and Yang Z 2023 Pressure-induced superconductivity in the photoelectric semiconductor BiSeI *Phys. Rev.* B **107** 1–8

[24] Hahn N T, Rettie A J E, Beal S K, Fullon R R and Mullins C B 2012 N-BiSI thin films: selenium doping and solar cell behavior *J. Phys. Chem.* C **116** 24878–86

[25] Murtaza S Z M and Vaqueiro P 2020 Rapid synthesis of chalcohalides by ball milling: preparation and characterisation of BiSI and BiSeI *J. Solid State Chem.* **291** 121625

[26] Dolcet Sadurni M, Timmo K, Mikli V, Volobujeva O, Mengü I, Krustok J, Grossberg-Kuusk M and Kauk-Kuusik M 2024 Preparation and characterization of SbSeI thin films *J. Sci. Adv. Mater. Devices* **9** 100664

[27] Caño I *et al* 2023 SbSeI and SbSeBr micro-columnar solar cells by a novel high pressure-based synthesis process *J. Mater. Chem.* A **11** 17616–27

[28] Bai R, Xiao B, Li F, Liu X, Xi S, Zhu M, Jie W, Zhang B B and Xu Y 2022 Growth of bismuth- and antimony-based chalcohalide single crystals by the physical vapor transport method *CrystEngComm* **24** 1094–9

[29] Kanchana G and Arivuoli D 2001 Spectroscopic investigation of BiSeI, SbSeI compounds and BiSbS$_x$Se$_{1-x}$I solid solutions *Indian J. Eng. Mater. Sci.* **8** 373–6 (available at: http://nopr.niscpr.res.in/handle/123456789/24465)

[30] Xu L *et al* 2024 2D BiSeI nanosheets for broadband self-powered photoelectrochemical photodetector *Phys. Status Solidi* **18** 1–9

[31] Hu H *et al* 2023 A mixed-dimensional quasi-1D BiSeI nanowire-2D GaSe nanosheet p-n heterojunction for fast response optoelectronic devices *Nanoscale Adv.* **5** 6210–5

[32] Li Y *et al* 2023 Polarization-sensitive photodetector based on high crystallinity quasi-1D BiSeI nanowires synthesized via chemical vapor deposition *Small* **19** 1–9

[33] Rawat D, Singh A, Singh N K and Soni A 2023 Anisotropic light-matter interactions in the single-crystal topological insulator bismuth selenide *Phys. Rev.* B **107** 2–7

[34] Deshpande M P, Bhatt S V, Sathe V, Rao R and Chaki S H 2014 Pressure and temperature dependence of Raman spectra and their anharmonic effects in Bi$_2$Se$_3$ single crystal *Physica* B **433** 72–78

[35] Martinez G *et al* 2017 Determination of the energy band gap of Bi$_2$Se$_3$ *Sci. Rep.* **7** 1–5

[36] Nechaev I A *et al* 2013 Evidence for a direct band gap in the topological insulator Bi$_2$Se$_3$ from theory and experiment *Phys. Rev.* B **87** 1–5

[37] Escobedo Morales A, Sánchez Mora E and Pal U 2007 Use of diffuse reflectance spectroscopy for optical characterization of un-supported nanostructures *Rev. Mex. Fís.* S **53** 18–22

[38] Levanyuk A P and Osipov V V 1981 Edge luminescence of direct-gap semiconductors *Sov. Phys.-Usp.* **24** 187–215

[39] Krustok J, Kaupmees R, Abbasi N, Muska K, Mengü I and Timmo K 2023 Bandgap fluctuations, hot carriers, and band-to-acceptor recombination in Cu$_2$ZnSn(S,Se)$_4$ microcrystals *Phys. Status Solidi* **17** 1–5

[40] Bleuse J, Perret S, Curé Y, Grenet L, André R and Mariette H 2020 Optical determination of the band gap and band tail of epitaxial Ag$_2$ZnSnSe$_4$ at low temperature *Phys. Rev.* B **102** 195205

[41] Fang H H, Adjokatse S, Shao S, Even J and Loi M A 2018 Long-lived hot-carrier light emission and large blue shift in formamidinium tin triiodide perovskites *Nat. Commun.* **9** 243

[42] Chepur D V, Bercha D M, Turyanitsa I D and Slivka V Y 1968 Peculiarities of the energy spectrum and edge absorption in the chain compounds AVBVICVII *Phys. Status Solidi* **30** 461–8

[43] Krustok J, Collan H and Hjelt K 1997 Does the low-temperature Arrhenius plot of the photoluminescence intensity in CdTe point towards an erroneous activation energy? *J. Appl. Phys.* **81** 1442–5

[44] Krustok J, Collan H, Hjelt K, Mädasson J and Valdna V 1997 Photoluminescence from deep acceptor-deep donor complexes in CdTe *J. Lumin.* **72–74** 103–5

[45] Krustok J, H S J, Collan H, Yakushev M, Mädasson J and Bucher E 1999 Origin of the deep center photoluminescence in CuGaSe$_2$ and CuInS$_2$ crystals *J. Appl. Phys.* **86** 364–9

[46] Krustok J, Raudoja J, Krunks M, Mändar H and Collan H 2000 Nature of the native deep localized defect recombination centers in the chalcopyrite and orthorhombic AgInS$_2$ *J. Appl. Phys.* **88** 205–9

[47] Krustok J, Raudoja J, Schön J H, Yakushev M and Collan H 2000 Role of deep donor-deep acceptor complexes in CIS-related compounds *Thin Solid Films* **361** 406–10

[48] Williams F 1968 Donor—acceptor pairs in semiconductors *Phys. Status Solidi* **25** 493–512